Received: 22 February 2024 | Revised: 10 April 2024 | Accepted: 12 May 2024

DOI: 10.1002/idm2.12194

RESEARCH ARTICLE

Interdisciplinary Materials — Open Access — WILEY

Ferroelectric catalytic $BaTiO_3$-based composite insoles to promote healing of infected wounds: Analysis of antibacterial efficacy and angiogenesis

Qiong Liu[1,2] | **Xudan Liu**[3] | **Linfeng Fan**[3] | **Xinna Bai**[3] | **Hao Pan**[3] | **Hang Luo**[1] | **Dou Zhang**[1] | **Haitao Huang**[2] | **Chris R. Bowen**[4]

[1]State Key Laboratory of Powder Metallurgy, Central South University, Changsha, Hunan, China

[2]Department of Applied Physics, The Hong Kong Polytechnic University, Hong Kong, China

[3]Department of Periodontics, Hunan Key Laboratory of Oral Health Research & Hunan 3D Printing Engineering Research Center of Oral Care & Hunan Clinical Research Center of Oral Major Diseases and Oral Health & Xiangya Stomatological Hospital & Xiangya School of Stomatology, Central South University, Changsha, Hunan, China

[4]Department of Mechanical Engineering, University of Bath, Bath, UK

Correspondence
Hao Pan, Department of Periodontics, Hunan Key Laboratory of Oral Health Research & Hunan 3D Printing Engineering Research Center of Oral Care & Hunan Clinical Research Center of Oral Major Diseases and Oral Health & Xiangya Stomatological Hospital & Xiangya School of Stomatology, Central South University, Changsha, Hunan 410008, China.
Email: panhao@csu.edu.cn

Dou Zhang, State Key Laboratory of Powder Metallurgy, Central South University, Changsha, Hunan 410083, China.
Email: dzhang@csu.edu.cn

Funding information
National Natural Science Foundation of China, Grant/Award Numbers: 52172265, 5230130435; Scientific research project of Hunan Provincial Department of Education, Grant/Award Number: 21B0009; Hunan Excellent Youth Science Foundation, Grant/Award Number: 2022JJ20067; State Key Laboratory of Powder Metallurgy, Central South University, Changsha, China;

Abstract

Our feet are often subjected to moist and warm environments, which can promote the growth of harmful bacteria and the development of severe infection in wounds located in the foot. As a result, there is a need for new and innovative strategies to safely sterilize feet, when shoes are worn, to prevent any potential foot-related diseases. In this paper, we have produced a non-destructive, biocompatible and convenient-to-use insole by embedding a $BaTiO_3$ (BT) ferroelectric material into a conventional polydimethylsilane (PDMS) insole material to exploit a ferroelectric catalytic effect to promote the antibacterial and healing of infected wounds via the ferroelectric charges generated during walking. The formation of reactive oxygen species generated through a ferroelectric catalytic effect in the PDMS-BT composite is shown to increase the oxidative stress on bacteria and decrease both the activity of bacteria and the rate of formation of bacterial biofilms. In addition, the ferroelectric field generated by the PDMS-BT insole can enhance the level of transforming growth factor-beta and CD31 by influencing the endogenous electric field of a wound, thereby promoting the proliferation, differentiation of fibroblasts and angiogenesis. This work therefore provides a new route for antimicrobial and tissue reconstruction by integrating a ferroelectric biomaterial into a shoe insole, with significant potential for health-related applications.

Qiong Liu and Xudan Liu contributed equally to this study.

the Hong Kong Polytechnic University, Grant/Award Number: 1-W34B

KEYWORDS
ferroelectric filed effect, PDMS-$BaTiO_3$ insole, piezo-catalysis, wound healing

1 | INTRODUCTION

Wound healing has emerged as one of the fundamental challenges confronting the medical community, given that skin wounds are often accompanied by bacterial infections.[1] Feet are frequently in contact with the ground and footwear and are often situated in a warm, humid, and relatively sealed environment, making them prone to significant bacterial growth. As a result, any wounds of the foot are often susceptible to infection. In addition, patients with certain diseases, such as peripheral artery disease, can experience impaired blood circulation in the feet, thereby leading to reduced wound healing capacity and a higher probability of infection and severe complications.[2,3]

In terms of wound healing, the correlation between infected skin wounds and the inherent endogenous electric fields of the skin is widely regarded as an important regulatory factor in the process of cell and tissue repair. During skin injury and infection, a complex series of biological potential changes occur in the body, including the formation of molecules and cell tissues that create internal electric fields.[4,5] In the human skin, the epidermis maintains a trans-epidermal potential of approximately 20–50 mV due to the Na^+/K^+ pump.[6] When the skin is subjected to trauma, a short circuit is created at the wound site, thereby resulting in a lower local wound potential than at the surrounding intact skin; this can lead to the formation of a lateral electric field that is directed from the surrounding intact and healthy skin towards the center of the wound.[7] This natural biological electric field has been shown to promote cell migration and the secretion of growth factors, thereby enhancing wound healing.[8] However, for patients with infected wounds, infection can lead to an inflammatory response that activates aerobic respiration and produces the release of electrons, which leads to changes in the electrical potential at the site of infection.[9] The lateral electric field at the wound site diminishes or even collapses, leading to an extended inflammatory phase of wound repair and ultimately a slowing down of the wound healing process.[10]

In this regard, the deformation of a ferroelectric material when subjected to an external force also leads to the generation of charge and an internal electric field. The ferroelectric charge can also lead to and the production of reactive oxygen species (ROS) if the charge can react with water molecules in the environment.[11–13] These ROS have been shown to exhibit antibacterial and anti-inflammatory effects, to aid in the suppression of infections and a promotion of the wound healing process.[14,15]

$BaTiO_3$ (barium titanate, BT) is a common lead-free ferroelectric and piezoelectric material with remarkable ferroelectric properties and high piezoelectric constants at room temperature; this is also coupled with no biological toxicity.[16–18] Polydimethylsiloxane (PDMS) is a common material used in conventional insoles, which has good chemical stability, anti-shear ability, and can be used for long periods at temperatures between −50°C and 200°C.[19,20] Combining these two materials therefore provides a route to create a piezoelectric insole that can generate charge during walking to produce ROS or an electric field.

In this paper, a BT piezoelectric material was added as a filler into a PDMS matrix to create biocompatible PDMS-BT composite insoles. When the ferroelectric composite insole is squeezed by the foot during human movement, it is able to produce electrons and holes.[16,21] By using the electrons and holes generated by the ferroelectric effect, self-antibacterial and self-sterilization properties can be realized on the insole, to reduce bacterial activity and effectively slow down biofilm formation. In addition, the regulatory role of electric field produced by the ferroelectric effect on wound healing has potential to lead to a variety of molecular and cellular interactions, and the mechanism of the impact of the electric field on infected wound healing was studied in detail. This novel concept of a ferroelectric insole provides a new approach for future therapeutic strategies related to antibacterial efficacy and angiogenesis.

2 | RESULTS AND DISCUSSION

A scanning electron microscopy (SEM) image of the microstructure of prepared PDMS insole is shown in Figure 1A, where the surface is a rough and exhibits a ridge-like structure. The BT nanoparticles, which are encapsulated in the PDMS matrix, mainly consist of irregular spherical particles with an average size of 0.6–1.0 μm, as shown in Figure 1B. The X-ray diffraction (XRD) data in Figure 1C shows the diffraction patterns of the synthesized PDMS and the PDMS-BT composite. The XRD pattern of the PDMS-BT mixture indicates that the peaks observed are in good agreement with those associated with the tetragonal structure of barium titanate (PDF #81-2203).[22] The BT

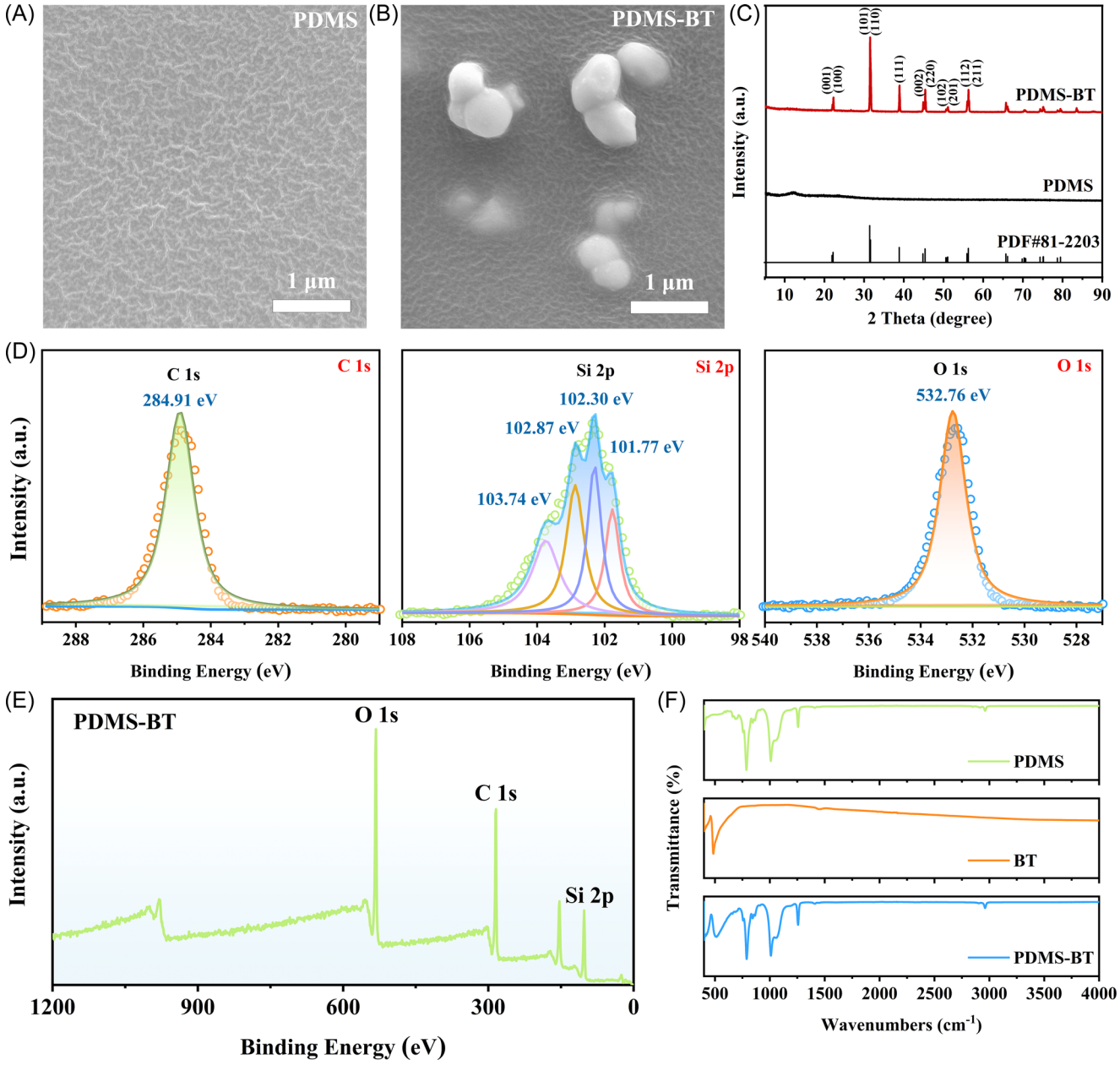

FIGURE 1 Scanning electron microscopy (SEM) images of (A) polydimethylsilane (PDMS) and (B) PDMS-BT. (C) X-ray diffraction (XRD) patterns of PDMS and PDMS-BT. (D) High resolution X-ray photoelectron spectroscopy (XPS) spectra of C 1s, Si 2p, O 1s and (E) full spectrum of PDMS-BT. (F) Fourier transform infrared spectroscopy (FTIR) spectra of PDMS, barium titanate (BT) and PDMS-BT.

appears to be a single phase with no secondary peaks, while the slight peak at approximately 12° can be indexed to the PDMS phase.[19] Furthermore, the phase structure of the BT is maintained after being introduced into the PDMS matrix.

High-resolution X-ray photoelectron spectroscopy (XPS) data of the PDMS-BT mixture are illustrated in Figure 1D,E. Due to the low content of BT on the surface of PDMS, the high-resolution spectra of Ba 3d and Ti 2p are difficult to observe. In Figure 1D, the peak of C 1s at approximately 284.91 eV belongs to carbon in the PDMS material. The Si 2p peak can be deconvoluted into four components, one at approximately 103.74 eV, which is related to the Si–O bond, and another two peaks at approximately 102.30 and 102.87 eV, which can be assigned to the Si–N bond; the final peak at 101.77 eV correspondings to SiO_x.[23,24] The peak located at 532.76 eV can be assigned to O 1s in PDMS.[25] Figure 1E shows the full XPS spectrum of the PDMS-BT composite, which indicates that the material is free of other impurities.

Fourier transform infrared spectroscopy (FTIR) was also carried out to accurately determine the structure of PDMS and the PDMS-BT composite. In the region from 4000 to 400 cm^{-1}, the bands located at approximately 788, 1009, and 1257 cm^{-1} are assigned to the PDMS phase. After BT has been added to the PDMS matrix, there is a new peak formed at approximately 500 cm^{-1}, which belongs to BT. No other impurity peaks were observed.

2.1 | Biocompatibility in vitro and in vivo

Understanding the biocompatibility of ferroelectric materials is crucial for their applications in the fields of medicine and bioengineering, especially in applications that make direct contact with human skin. When evaluating the cytotoxicity of PDMS-BT, we selected human skin epithelial cell lines HaCat cells and the mouse fibrosis cell lines L929 cells. We used a live/dead staining assay to evaluate the cytotoxicity of PDMS-BT. In this experiment, by observing the number and proportion of stained cells under a fluorescence microscope, we are able to assess the survival and death of cells. As shown in Figure 2A,B, after 48 h of co-incubation, the HaCat cells and L929 cells in the control group, PDMS group, and PDMS-BT group all exhibited a healthy morphology, and only a small amount of dead red cells. The cytotoxicity of all groups to cells can be neglected, indicating that these materials have good biocompatibility. Then, the number of viable cells was calculated using ImageJ, where the results showed that the cell vitality of all groups remained above 95%.

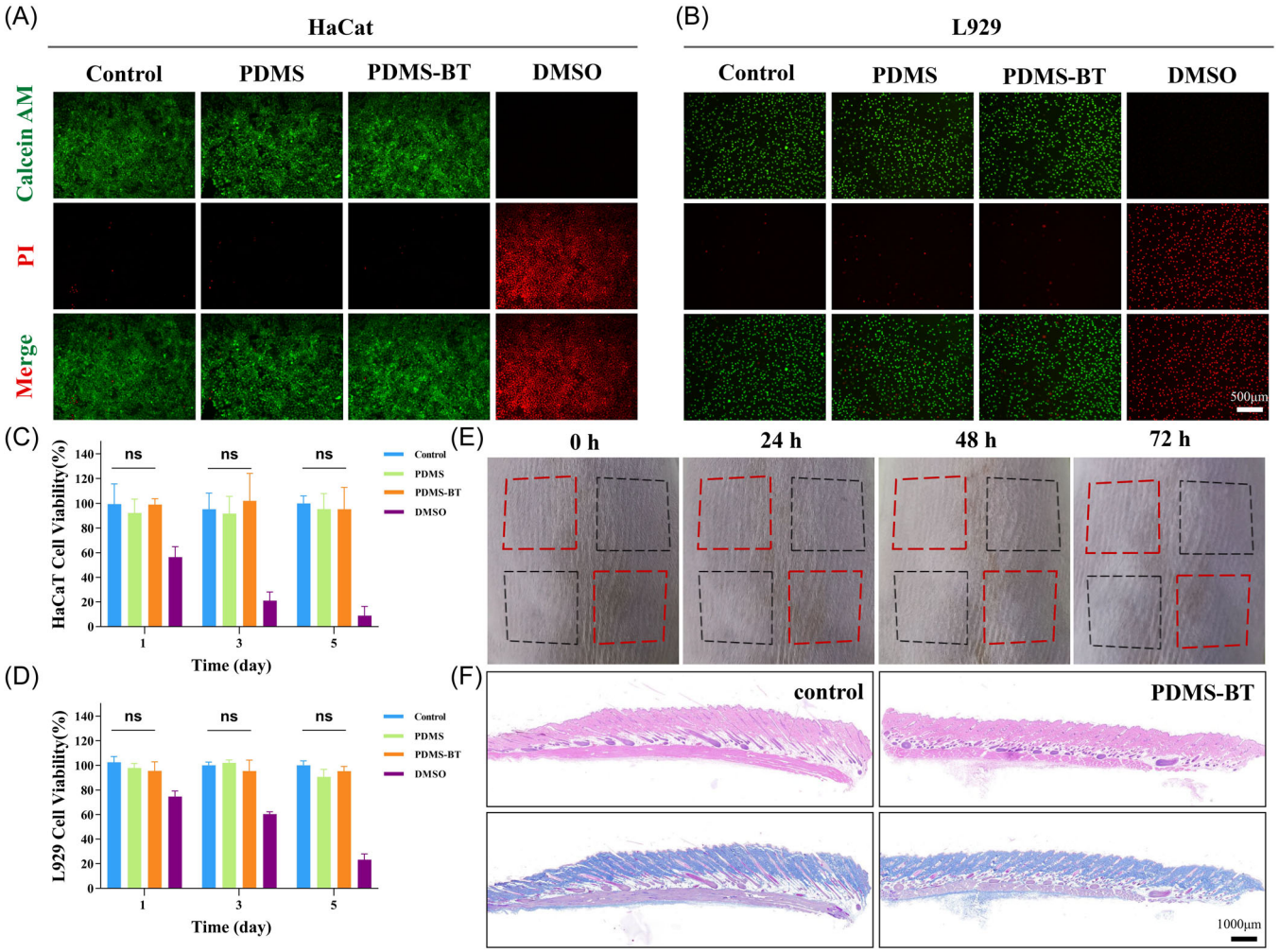

FIGURE 2 Cytotoxicity and skin irritation. Live/dead staining of (A) HaCat cells and (B) L929 cells treated with different groups. Cell viability assay with CCK-8 for (C) HaCat cells and (D) L929 cells. Following the application of the PDMS-BT membrane to the hairless skin surface of rats and ultrasonic stimulation, (E) representative skin images were acquired, and (F) the pathological assessment was conducted after 72 h. Data represent mean ± SD. BT, barium titanate; DMSO, dimethylsulfoxide; ns, no statistical significance; PDMS, polydimethylsilane.

To quantitatively evaluate the cytotoxicity, we used a commonly used CCK-8 assay. As shown in the CCK-8 data in Figure 2C,D, both the HaCat cells and L929 cells showed no significant difference in cell viability after 1, 3, and 5 days of culture in the PDMS-BT group compared with the group and the PDMS group, and the cell viability was over 80%. This indicates that the cytotoxicity of PDMS-BT to these two types of cells can be neglected, and this is consistent with the results of the live/dead staining assay, further confirming that PDMS-BT has low cytotoxicity. In this experiment, dimethylsulfoxide (DMSO) was used as a positive control group, which showed significant cytotoxicity to verify the normal performance of the cells used in the experiment in terms of both sensitivity and reactivity. The low cytotoxicity exhibited by PDMS-BT material can be attributed to the good biocompatibility of both PDMS and BT materials in its composition.[26,27]

To evaluate the skin irritation characteristics of PDMS-BT, we conducted a skin irritation experiment (Supporting Information S1: Figure S1). As shown in Figure 2E, neither the control group nor the test area covered with the PDMS-BT material showed any signs of erythema or edema on the skin. When we removed the sample, and the skin erythema and edema scores were close to zero. In addition, the hematoxylin and eosin (H&E) staining and Masson staining images of the evaluation area showed no inflammatory lesions or significant histopathological abnormalities (Figure 2F). These systematic experimental results indicate that the PDMS-BT has biological safety for skin contact.

2.2 | Cell migration and angiogenesis in vitro

To investigate the migration ability of L929 cells cocultured with different samples, a scratch test was applied (Figure 3A). As Figure 3B shows, after co-incubation of 24 h, the percentage healing of cells for the control, PDMS, and PDMS-BT groups were 69.40 ± 4.32%, 72.07 ± 6.70%, 89.72 ± 2.26%, respectively. A tubule formation assay was

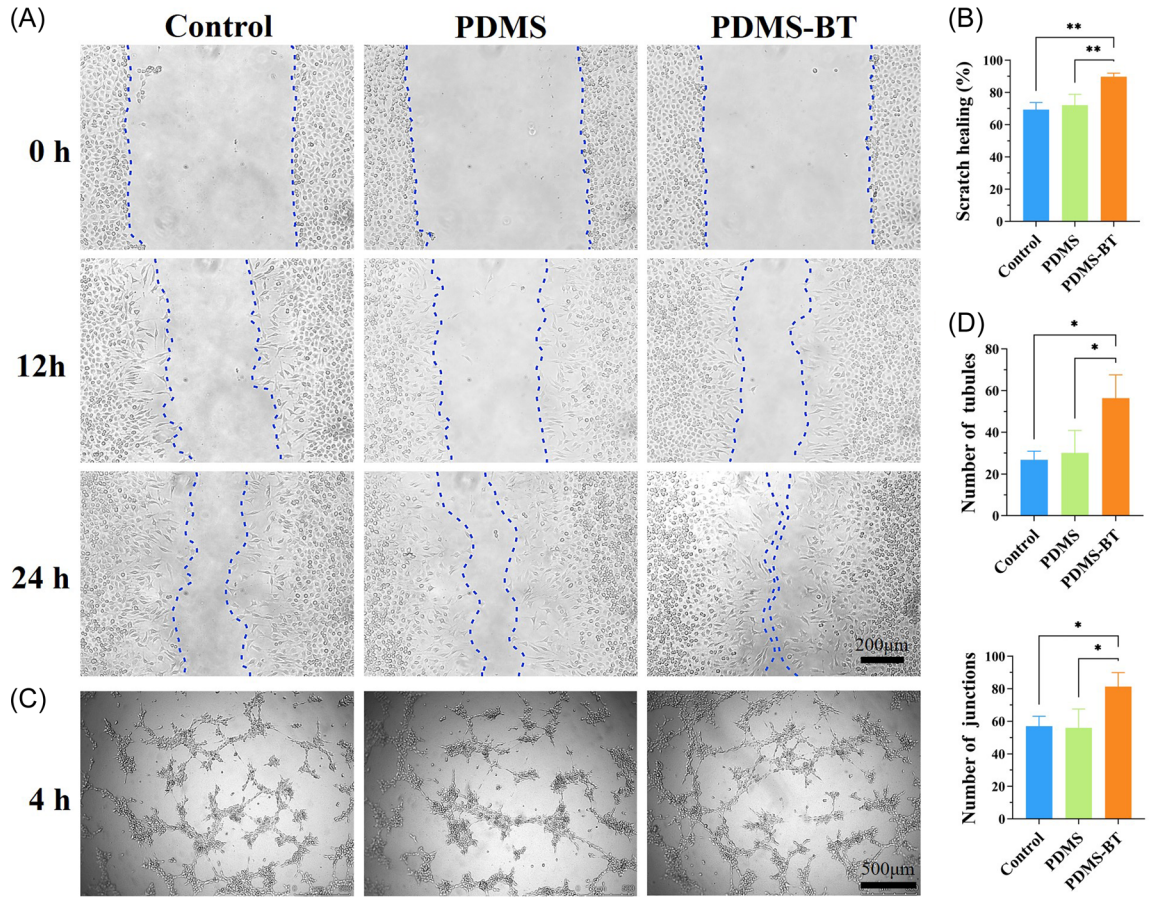

FIGURE 3 Migration and angiogenesis in vitro. (A) Representative images of wound scratch healing assay for L929 at different times. (B) Quantification of L929 cells migration. (C) Tube formation of HUVECs on Matrigel after incubation with different groups for 4 h. (D) Number of tubules and number of junctions in randomly selected fields. Data represent mean ± SD. BT, barium titanate; DMSO, dimethylsulfoxide; PDMS, polydimethylsilane. *$p < .05$; **$p < .01$.

conducted to evaluate the effects of different samples on the angiogenic potential of HUVECs (Figure 3C). The number of tubules and number of junctions, Figure 3D, were used to quantify the formed tube network. Compared with the control group and PDMS group, the HUVEC incubated with PDMS-BT exhibited enhanced activity in terms of new vessel formation, with a significant increase in angiogenesis of more than 20%. The results suggest that PDMS-BT under ultrasonic (US) stimulation not only has a high biocompatibility for cell viability but also exhibits high biological activity for promoting the migration of L929 and the angiogenesis of HUVEC in vitro.

These are resulted from the small electric fields generated by the PDMS-BT composite when subjected to dynamic external forces. This electric field can act directly on surrounding cells, thereby affecting ion channels and receptors on the cell membrane, and altering the intracellular potentials.[28] The effect of this electric field can regulate the activity, polarity, and migration of cells, thus affecting cell migration and angiogenesis.[29]

2.3 | Antibacterial activity evaluation in vitro

To evaluate the antibacterial activity of the PDMS-BT material, we selected *Escherichia coli* (*E. coli*) and *Staphylococcus aureus* (*S. aureus*) as model strains of Gram-negative and Gram-positive bacteria, respectively. An agar plate counting method was employed to assess the bacterial colony count. The antibacterial performance of the different samples is shown in Figure 4. Notably, in the PDMS-BT group treated with ultrasound for 20 min, the viability of *E. coli* was only 44.7%, and that of *S. aureus* was lower at 24.0%. In contrast, there was no significant difference between the PDMS group and the control group (Figure 4A). This suggests that the application of ultrasound can stimulate the antibacterial properties of PDMS-BT, which is associated with the addition of BT filler. Furthermore, we subjected the ferroelectric PDMS-BT material to mechanical impacts using a reciprocating machine to simulate the mechanical stress encountered by insoles during real-time walking. As evident from Figure 4B, there was a positive correlation between the duration of impact and the antibacterial efficacy. After 1 h of mechanical impacts, the viability of *S. aureus* was only 28.2%, and after 2 h of impact, its viability significantly decreased to 11.1%. Similar trends were observed for *E. coli*. This indicates that the antibacterial properties of the PDMS-BT material are effectively stimulated under simulated insole compressive impacts. Notably, after 60 h of impact on the material, we conducted the same antibacterial testing procedure, and the resulting bacterial colony count is shown in Supporting Information S1: Figure S2. Under the applications of repeated impacts, the bacterial colony count of *E. coli* and *S. aureus* co-cultured with PDMS-BT for 2 h was significantly lower than in control and PDMS. This suggests that the PDMS-BT maintains its antibacterial effect even after prolonged mechanical stress. A purely US treatment only exhibited a minor antibacterial effect, which was attributed to its mechanical damage and cavitation effects. In contrast, PDMS-BT exhibited a stronger antibacterial capability compared to control and PDMS and is attributed to its ferroelectric charge and catalytic effects after mechanical stimulation.

Subsequently, to evaluate the antibacterial biofilm resistance of the PDMS-BT material, crystal violet staining was employed on biofilms of *E. coli* and *S. aureus* to quantifying the anti-biofilm activity of PDMS-BT. Figure 4C shows the microscopic images of these biofilms after US treatment under co-cultivation with different materials, with a positive correlation between bacterial biomass and staining depth. In the control group and the PDMS group, deeper-stained biofilms were observed. In contrast, only minor biofilm fragments were observed in the PDMS-BT group. Through quantitative analysis of the stained biomass, it was found that nearly 80% of the *E. coli* biofilm was disrupted after treatment with PDMS-BT (Figure 4G). To detect the bacterial viability on the material surface, further Alamar Blue staining was conducted, where the viability of both bacteria decreased by approximately 75% (Figure 4H). These staining results indicate that the PDMS-BT composite can reduce bacterial activity and effectively slow down biofilm formation during ultrasound stimulation. It can be inferred that the surface charge separation and distribution of the electric potential on the PDMS-BT surface after the application of a mechanical stress may break the balance and stability of bacterial surface charges, and disrupt the charge balance between bacteria and the surrounding environment; this can therefore affect the bacterial adhesion properties and the survival environment, ultimately leading to difficulties in biofilm formation and a reduced bacterial viability on the material surface.[30]

To further determine whether the death and suppression of bacteria are related to ROS, we utilized an active oxygen detection kit (reactive oxygen species assay kit) to examine the bacterial biofilms post-experiment, where the bacteria with reactive oxygen is detected via green fluorescence. As shown in Figure 4D, the PDMS-BT group exhibited a more scattered distribution of green fluorescent regions, while for the control group, almost no fluorescence was detected. We have included high-resolution images in Supporting Information S1: Figures S3 and S4 to provide a clear visualization of the ROS generation. This suggests that ROS are generated and

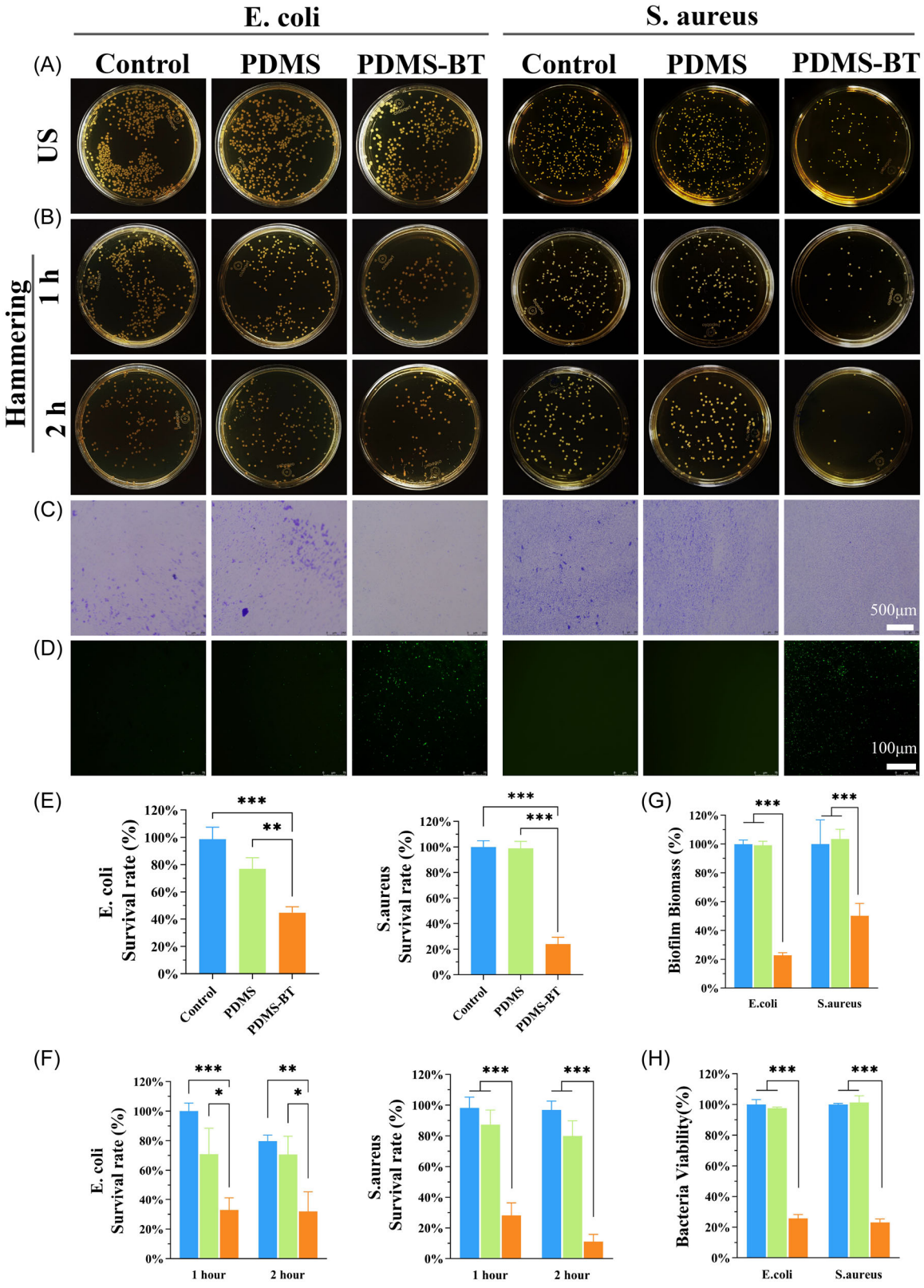

FIGURE 4 Antibacterial activity of PDMS-BT in vitro. (A) Representative images of *Escherichia coli* (*E. coli*) and *Staphylococcus aureus* (*S. aureus*) colonies with different treatment with ultrasonic (US) irradiation. (B) Representative images of *E. coli* and *S. aureus* colonies after 1 h/2 h mechanical impacting of different samples using a reciprocating machine. (C) Representative images of crystal violet-stained biofilm and (G) biofilm biomass of *E. coli* and *S. aureus*. (D) Fluorescence detection of reactive oxygen species in bacterial biofilms. (E) Quantitative analysis of bacterial survival rate in (A). (F) Quantitative analysis of bacterial survival rate in (B). (H) Activity of *S. aureus* and *E. coli* on the surface. To enhance the visual effect, the bacterial colonies images have been color-modified. Data represent mean ± SD. BT, barium titanate; PDMS, polydimethylsilane. *$p < .05$; **$p < .01$; ***$p < .001$.

accumulated within the bacteria for the PDMS-BT group. In addition, 5,5-dimethyl-1-pyrroline-*N*-oxide (DMPO) was selected as the free radical trapping agent to further confirm the existence of ROS during the ferroelectric catalytic process. Supporting Information S1: Figure S5 illustrates a standard equidistant and quadrupled peak with the peak height of 1:2:2:1, which belongs to a typical electron spin resonance (ESR) spectrum for DMPO-•OH.[31] Supporting Information S1: Figure S6 shows a typical ESR diagram of DMPO-•O_2^- with a sixfold peak, which is produced by the PDMS-BT and PDMS. The peak height of both DMPO-•OH and DMPO-•O_2^- produced by PDMS-BT is significantly higher than that of PDMS, and there is no peak produced for the pure water, which further verified the better antibacterial performance of PDMS-BT. The antibacterial effects of reactive oxygen have been described through oxidation of bacterial cell wall polysaccharides and proteins, damage to bacterial membrane lipids, and disruption of the structural and functional integrity of bacterial proteins.[32,33] The marginally superior antibacterial effect observed in *S. aureus* compared to *E. coli* can be ascribed to two main aspects: firstly, the differential reactivity of •O_2^- and •OH with biomolecules, and secondly, the structural differences between Gram-positive and Gram-negative bacteria. Gram-negative bacteria are characterized by the presence of an outer membrane and a peptidoglycan layer, whereas Gram-positive bacteria lack such an outer membrane. This discrepancy may influence their sensitivity to ROS, rendering them more prone to ROS-induced damage.

In the antibacterial portion of this experiment, the most common strains were selected to evaluate the efficacy of our ferroelectric system, and the effects were notably substantial. Bacteria differ among various human body sites. In future research, special strains from different areas will be tested using this antimicrobial system, thus providing a greater data foundation to support clinical antibacterial efforts.

2.4 | In vivo infected wound healing

The model of wound healing in the back of rats is selected and designed to simulate the clinical conditions of wound infection in humans. By creating wounds on the back of rats and allowing them to become infected, this experimental model enabled the evaluation of the antibacterial properties of the materials to study the wound healing process (Figure 5A). In this study, we successfully established a rat full-thickness skin wound

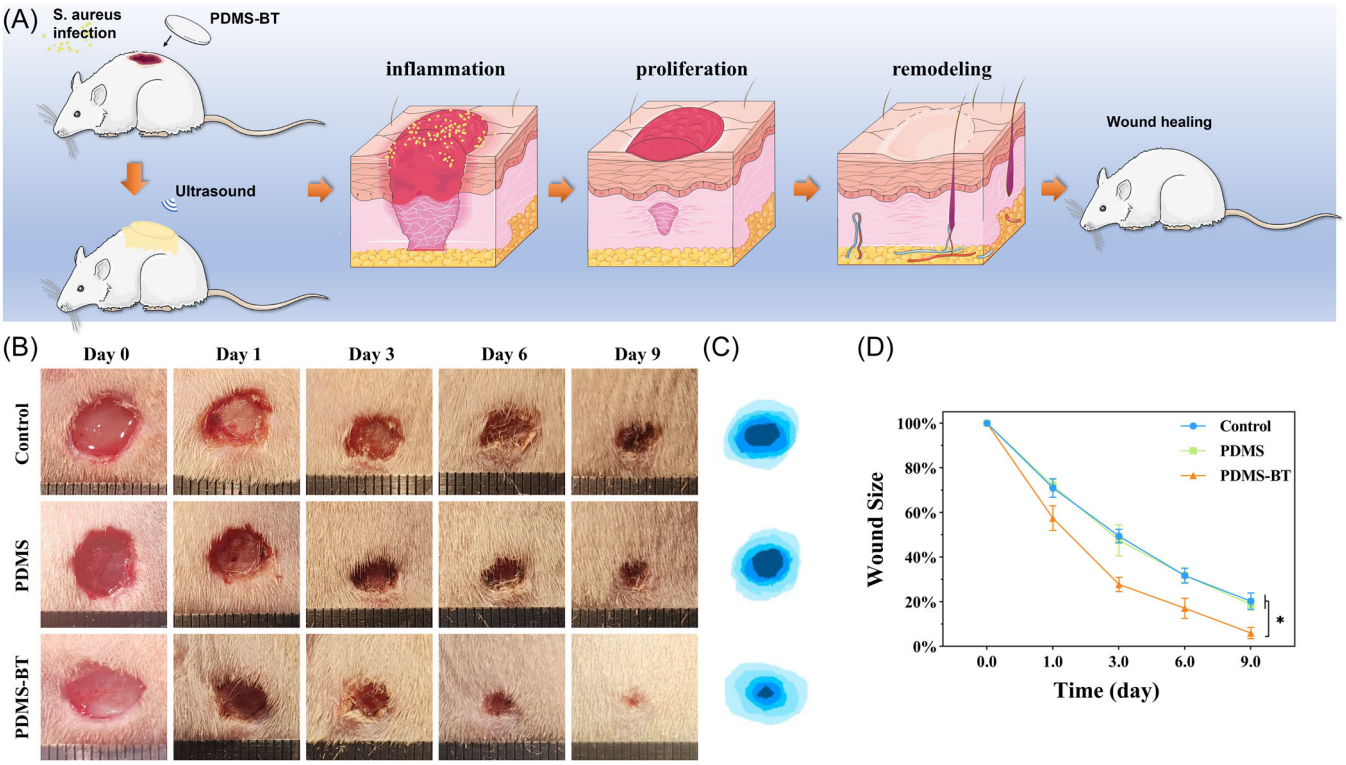

FIGURE 5 (A) Schematic of PDMS-BT for treating infectious wounds in rats. (B) Representative photographs of infected wounds at different times during the treatment. (C) Schematic of wound closure trace during 9 days period. (D) Quantitative data of relative wound area at different time points. Data represent mean ± SD. BT, barium titanate; PDMS, polydimethylsilane. *$p < .05$.

model that was infected with *S. aureus* to investigate the in vivo anti-infective potential of PDMS-BT and its effects on wound healing. After 24 h of wound modeling, distinct yellow pus and a pseudomembrane were observed, indicating the successful establishment of the wound infection model (Supporting Information S1: Figure S7a). All groups were subjected to smear preparation of a wound exudate after 1 day of contact with the wound. The results indicate that bacterial infections in the wounds were detected in all groups, but the suppurative inflammation essentially vanished, and this is likely to be attributed to the strong self-healing properties of the rats. The PDMS-BT group exhibited an antibacterial function during US stimulation, demonstrating in vivo anti-infective properties, significantly alleviating wound infection, as confirmed by standard swab culture and agar plate count (Supporting Information S1: Figure S7b). On Days 0, 1, 3, 6, and 9, images of these wounds were taken to observe the progress of repair (Figure 5B). On Day 9, the wound defects in the PDMS-BT group were almost healed, and a shallow pink scar appeared. Meanwhile, the control group and the PDMS group still had prominent dark blood scabs, suggesting persistent inflammatory infiltration and the absence of interstitial filling. The wound closure simulation diagram, Figure 5C, drawn based on the digital images of the healed wounds shows that skin regeneration in the PDMS-BT group was significantly faster than that in the control group. We have recorded and analyzed the process of wound healing area changes (Figure 5D), where the average wound area of the PDMS-BT group on Day 3 is approximately 27.8%, which is smaller than the control (49.4%) and PDMS group (47.6%). As the time increases to Day 9, the PDMS-BT group maintains the best condition with the wound area reaching $6.0 \pm 2.5\%$, while the PDMS group and control group have larger areas of $18.9 \pm 2.6\%$ and $20.3 \pm 3.6\%$, respectively. The wounds treated with PDMS-BT healed the fastest, with a noticeable difference from the other two groups on Day 3. By Day 9, the wound contraction reached approximately $7.3 \pm 2.5\%$ for the PDMS-BT group, and this is likely to be due to the onset of antibacterial effects, which accelerated the removal of bacteria from the wound site, thereby initiating the tissue reconstruction process more rapidly. In contrast, the wound healing rates of the control group and the PDMS group were slower, with a maximum relative wound area on Day 9, and the contraction reaching approximately 20%. Statistical comparisons between the control group and the PDMS group showed no significant differences in healing rates ($p > .05$). In addition, the SEM and XRD of PDMS-BT after hammer and US experiments have no obvious difference with the original PDMS-BT as shown in Supporting Information S1: Figures S8 and S9, which indicates the excellent structural stability of PDMS-BT insoles.

2.5 | Histopathologic evaluations of collagen deposition and angiogenesis

To further analyze the epidermal regeneration and wound repair processes, we conducted H&E staining on the newly formed tissue at the wound site (Figure 6A). The scars formed by skin wounds are often considered failures of regeneration if there is no functional reconstruction, such as the presence of newly formed hair follicles. We observed that the subcutaneous tissue in the PDMS-BT group contained abundant hair follicles, as indicated by the yellow stars in Figure 6. On Day 9, the epidermal thickness in the PDMS-BT group was deeper than those in other groups. In terms of the rate of wound healing, the regenerated epithelial tissue in the PDMS-BT group was thicker and more regular, with a significant number of newly formed hair follicles (Figure 6C). This suggests that it possesses good antibacterial properties and can improve the microenvironment for wound healing. In contrast, the control group and PDMS group exhibited incomplete epithelial structures, and the skin architecture was not clearly established.

We utilized the Masson staining method to assess the distribution of collagen in the wound area (Figure 6B). The gaps between the granulation tissues are denoted by red arrows, and it was observed that the width of the granulation tissue in the PDMS-BT group was significantly narrower than that in the control group and PDMS group, with no significant statistical differences observed between them (Figure 6D). Collagen, as a crucial component of the skin, plays a pivotal role in wound healing, where its synthesis, deposition, and direction of arrangement are crucial for the healing process. As shown in Figure 6E, the PDMS-BT group exhibited greater collagen deposition, presenting a distribution of numerous dark blue fibers. On Day 9, the collagen deposition rate in the PDMS-BT group reached $44.3 \pm 8.0\%$, with a more organized arrangement. This phenomenon suggests that the PDMS-BT group is more capable of reshaping the extracellular matrix and promoting the reconstruction of the epithelial tissue. In contrast, there were no significant differences between the control group and PDMS group, with incomplete epithelialization and the presence of a large area of immature granulation tissue deposition around the wound. The collagen deposition rates for the control and PDMS groups were lower than PDMS-BT groups at $23.8 \pm 8.1\%$ and $25.8 \pm 3.3\%$, respectively.

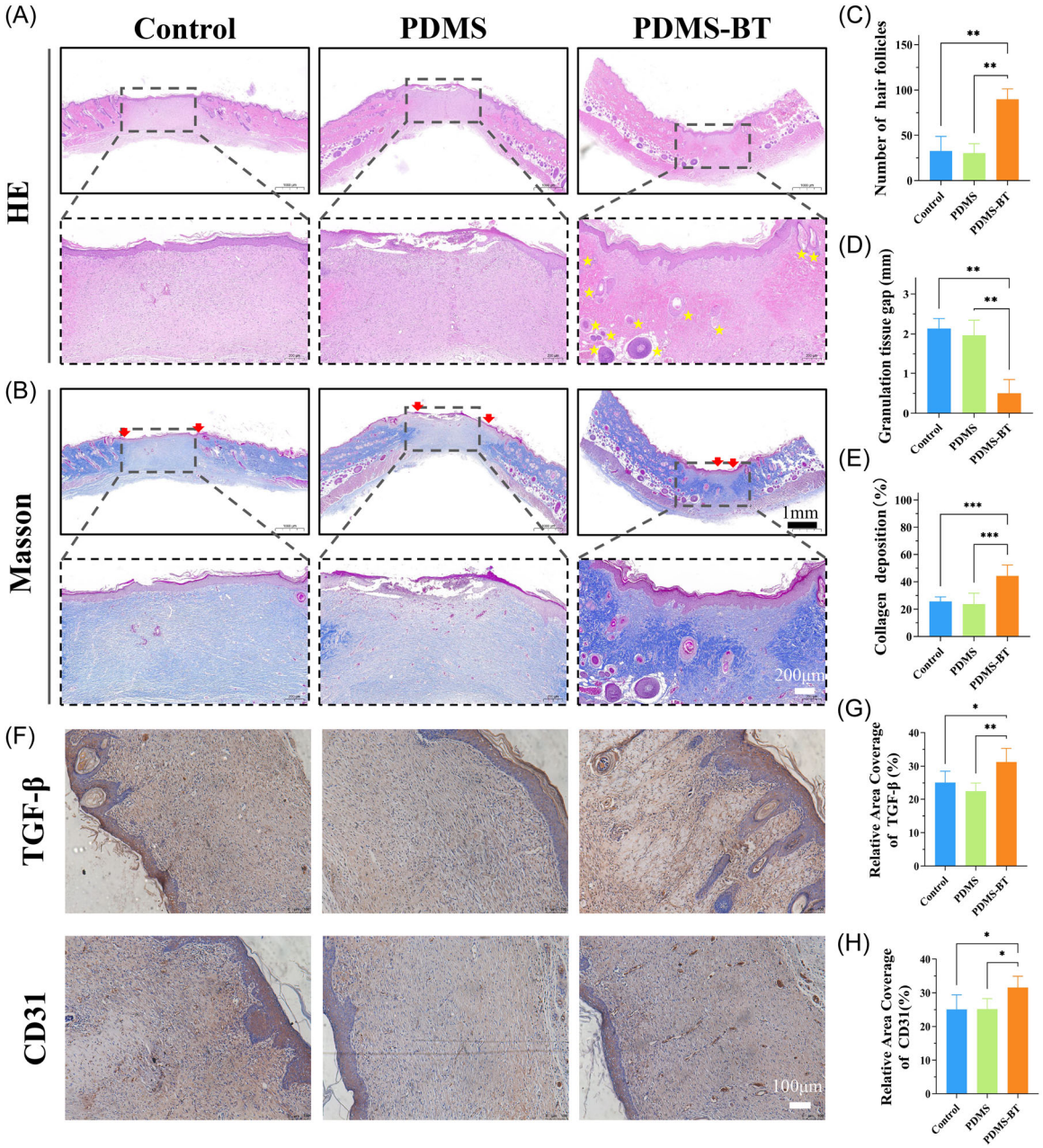

FIGURE 6 In vivo study on the effects of PDMS-BT on collagen deposition and angiogenesis. (A) Representative images of wound tissue sections in different groups stained by hematoxylin and eosin. (B) Representative images of wound tissue sections in different groups stained by Masson. Hair follicles are marked with yellow stars, and the two red arrows represent the granulation tissue gaps. Quantification of (C) hair follicle count, (D) granulation tissue gap, and (E) collagen deposition. (F) Representative immunohistochemical images of TGF-β and CD31. Quantitative data of the relative area coverage of (G) TNF-β and (H) CD31. All data are sourced from the ninth day of wound healing. Data represent mean ± SD. BT, barium titanate; PDMS, polydimethylsilane; TGF-β, transforming growth factor-beta. *$p < .05$; **$p < .01$; ***$p < .001$.

The infection of wounds can inhibit the proliferation and migration of fibroblasts, thereby delaying the healing rate of the wound. Furthermore, bacterial infection can also hinder the formation of new blood vessels, thereby affecting the blood supply and oxygen delivery to the wound, and negatively impacting the healing process. To investigate the biological mechanisms of PDMS-BT in wound repair, the protein expression levels of transforming growth factor-beta (TGF-β) and CD31 were selected as evaluation indicators. TGF-β is an important cytokine that can promote the activation and proliferation of fibroblasts, and can stimulate collagen synthesis and epithelial cell proliferation, which is beneficial for wound repair and tissue regeneration processes. In contrast, CD31 is a marker for vascular endothelial cells, which are involved in regulating the angiogenesis

process and promoting the formation and growth of new blood vessels. Through immunohisto-chemical staining images, as shown in Figure 6F, we observed a significant increase in the immunohisto-chemical staining intensity and expression level of TGF-β in the dermal cell layer in the PDMS-BT group, which shows a statistical difference from the control groups and PDMS groups in Figure 6G. This suggests that PDMS-BT may promote the activation and proliferation of fibroblasts by regulating the TGF-β signaling pathway. In addition, in the tissue samples of the PDMS-BT group, we observed a significant increase in the number of vascular endothelial cells positive for CD31. This indicates that PDMS-BT promotes the process of angiogenesis and is consistent with our previous in vitro cell experiments.

Lastly, morphological observations were conducted on major organs such as the heart, liver, spleen, lung, and kidney to assess the long-term biological safety of PDMS-BT (Supporting Information S1: Figure S10). Similar to the control group, no significant lesions or other histopathological abnormalities were observed in the tissue sections from the PDMS-BT group.

To summarize, the healing of infected wounds is a complex biological process, which is closely linked to the regulation of bacterial infection in wounds and the promotion of cell proliferation, differentiation, and migration around the wound site.[34–36] First, the PDMS-BT exhibits antibacterial properties under the action of mechanical stress to inhibit bacterial growth in wounds, thereby reducing bacterial vitality. This effect helps mitigate the negative impact of infection on wounds and creates favorable conditions for wound healing.[37] Second, the PDMS-BT composite can also regulate the electrical microenvironment of skin wounds, thereby enhancing the expression and secretion of TGF-β and CD31 in the wound, accelerating the proliferation and migration of fibroblasts, promoting re-epithelialization and granulation formation, as well as promoting the formation of new blood vessels and collagen deposition.[38,39] Ultimately, these actions accelerate the overall wound healing process.

Images of the PDMS-BT flexible insole are shown in Supporting Information S1: Figure S11, which has a length of 240 mm, a largest width of 100 mm and a thickness of 10 mm. The insole possesses mechanical properties that are appropriate to allow it to be flattened and then return to its original shape under repeated mechanical squeezing during loads similar to walking. Finite element modeling (FEM) was used to predict the ferroelectric potential produced by PDMS-BT insole during conditions associated with walking. Figure 7A shows the distribution of stress in the PDMS-BT insole when a mechanical force (based on a force of 300 N, assuming a body mass of 60 kg distributed over two feet) is applied along the negative z axis. As can be seen from Figure 7A, in the case of uniform force applied to the insole surface, the BT nanoparticles near the edge of the insole are affected by the fixed soles, and the surface stress on the BT nanoparticles in the center is relatively small since PDMS is a highly flexible and compliant material. Figure 7B illustrates the distribution direction of the internal stress field between the upper and lower surfaces of pristine PDMS-BT. Figure 7C shows FEM results of the ferroelectric voltage based on the direction of the polarization electric field is along the z axis, which is approximately 14.4 V during a walking condition during total bottom-face contact.

To directly measure the ferroelectric response of the BT particles, the ferroelectric properties of the BT nanoparticles was verified by atomic force microscopy (AFM) with a piezoresponse force microscopy (PFM) module, as shown in Figure 7D–I, and the short-circuit transfer charge, output voltage and current of PDMS-BT under 100 N at 1 Hz are shown in Supporting Information S1: Figures S12 and S13. The three-dimensional (3D) AFM morphology of BT is irregular shape, and the corresponding height curve matches well the SEM results shown in Figure 1B, which is approximately 800 nm in diameter. To verify the enhancement of catalytic performance due to the addition of BT to PDMS, Kelvin probe force microscopy was employed to identify the piezoelectric potential of the pure BT nanoparticles. An inhomogeneous potential distribution is displayed on $BaTiO_3$, and the contact potential difference between the nanoparticle and the tip is approximately 8.0–10.2 μV, the corresponding surface potential along the white line in Figure 7F is shown in Figure 7G. As shown in Figure 7H, the strain-electric field (S-E) response of BT is related to the variation of PFM amplitude with tip bias voltage. The maximum amplitude of the deformations in BT is approximately 6.5 pm, and the hysteresis loop is a well-defined PFM butterfly loop that exhibits a clear variation in amplitude. The phase angle, as shown in Figure 7I, in the local hysteresis loop changes by 160° and reveals the non-zero remnant polarization or ferroelectric nature of BT,[40] which originates from the displacement of the Ti^{4+} cation from the center of the oxygen octahedron in BT.[41]

Figure 8 illustrates the synthesis procedure and application of the PDMS-BT material and insole, and the mechanism for ferroelectric-catalysis promoting infected wound healing with PDMS-BT insole. When the skin surface is not injured, the intact epidermis primarily relies on the active inflow of Na^+ to form a positive transepithelial potential difference on the basal layer side and a negative potential on the stratum corneum side. When the skin is damaged, the high resistance of the injured epidermis is destroyed, resulting

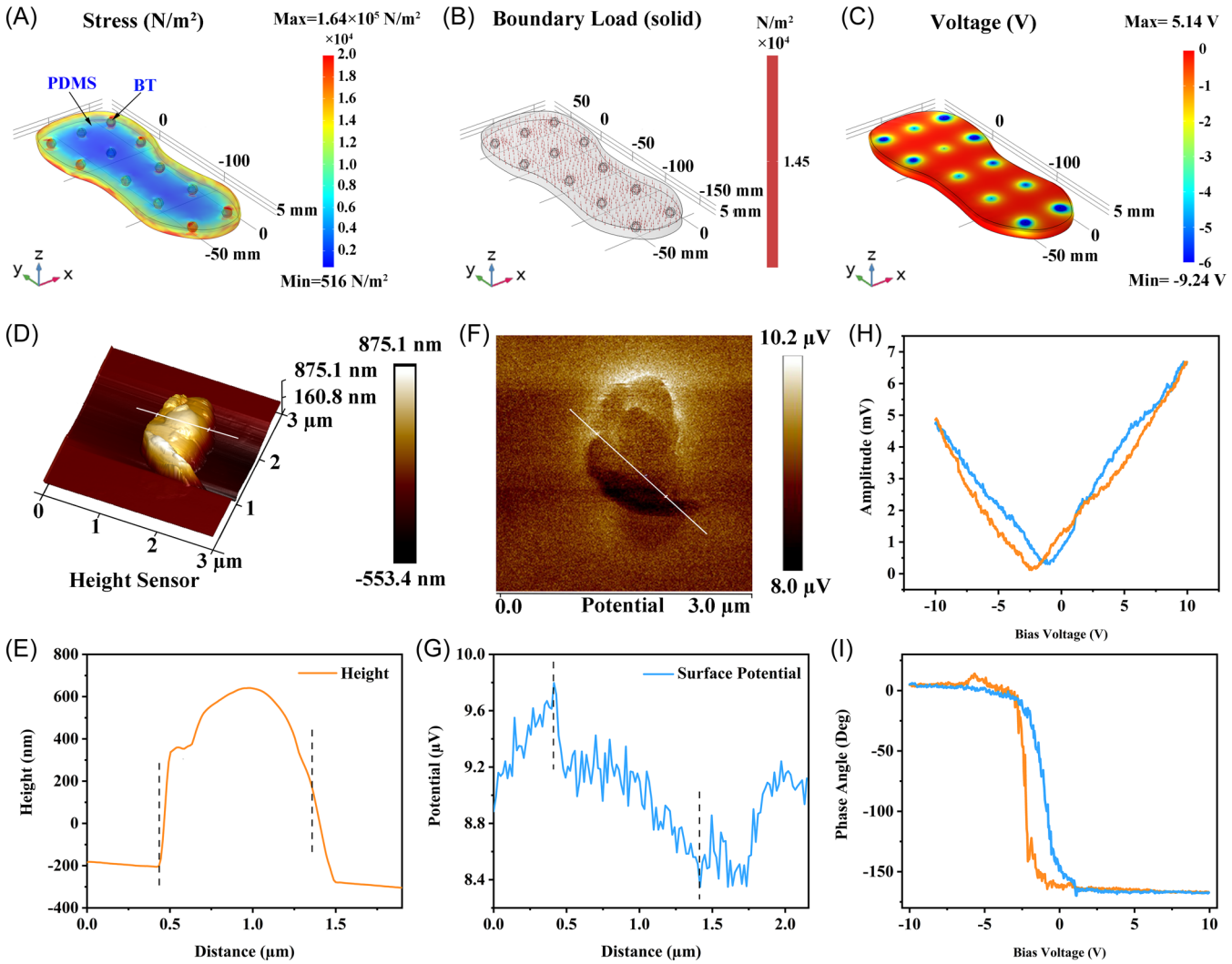

FIGURE 7 (A) Finite element model simulation result of PDMS-BT under the application of force in the *z*-direction. (B) Corresponding boundary load spectra and (C) piezoelectric voltage formed at the insole. Piezoelectric and ferroelectric characterization of barium titanate (BT): (D) three-dimensional topology image of atomic force microscopy and (E) the corresponding height curve, (F) Kelvin probe force microscopy phase image and (G) the corresponding surface potential distribution, (H) piezoresponse force microscopy (PFM) amplitude butterfly loops and (I) PFM phase hysteresis loops of BT nanoparticles. PDMS, polydimethylsilane.

in a local epidermal current short circuit, and the transepithelial potential difference at the injured site is reduced to 0 mV.[42] The transepithelial potential difference of the epidermis near the injury remains at a normal level, so that a stable lateral potential gradient and subepidermal injury current is generated along the epidermal plane to promote wound healing. However, for patients with infected wounds, the lateral electric field of the wound is weakened or even tends to vanish, which leads to a prolonged inflammatory period of wound repair and slows down the rate of wound repair. The electric field generated by the PDMS-BT during walking can induce the formation of electric charge through ferroelectric effect, so that it can react with water molecules to generate ROS group for antibacterial, which can limit wound infection and promote wound healing. On the other hand, the formation of ferroelectric-based electric field is equivalent to applying an external electric field on both sides of the surface skin. When the direction of the applied electric field is consistent with the direction of the wound endogenous electric field, the rate of cell migration around the wound is accelerated, thus accelerating the wound healing.

3 | CONCLUSION

In summary, we have developed a novel antibacterial insole which promotes the healing of infected wounds by exploiting the ferroelectric catalytic effect. Detailed

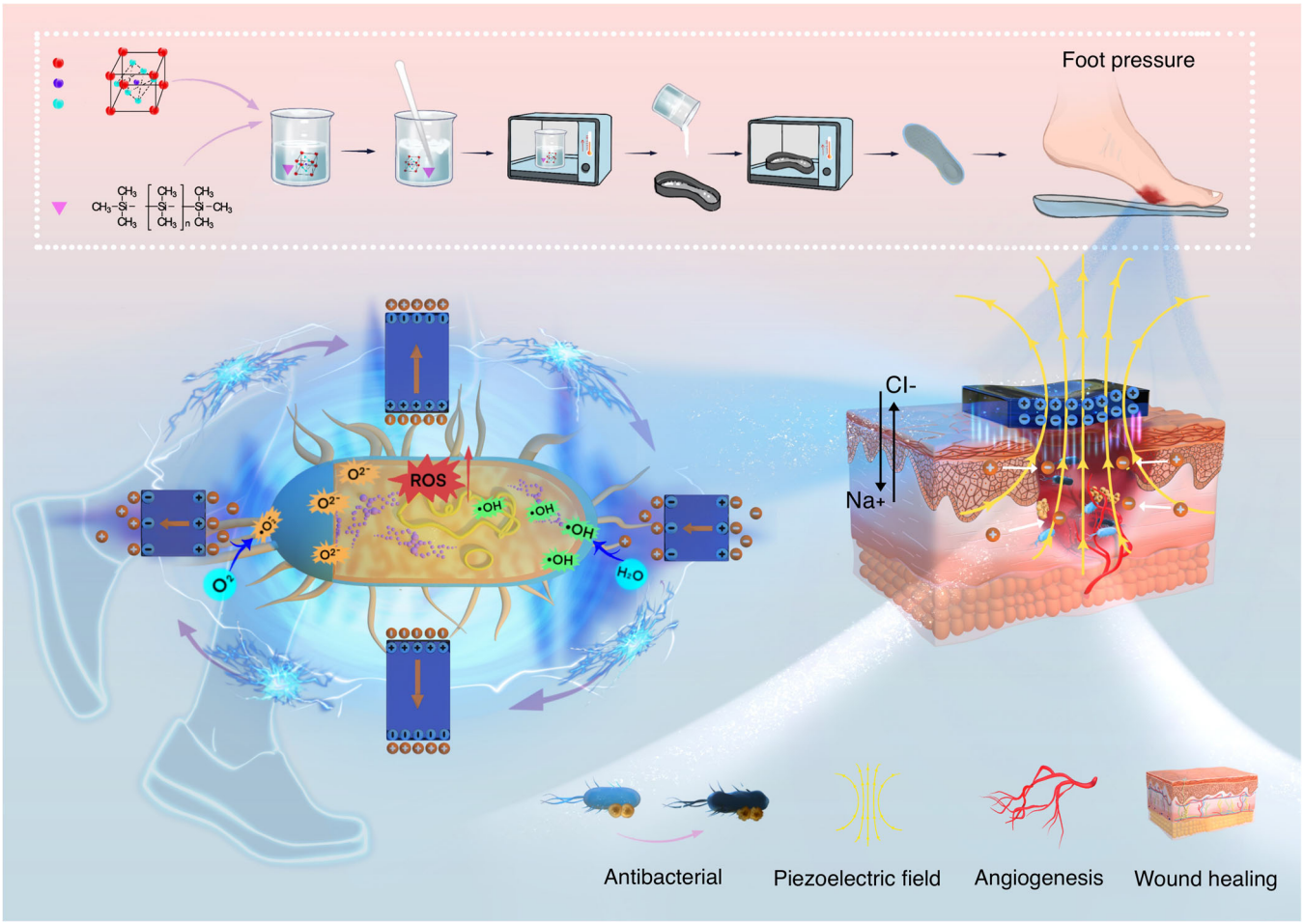

FIGURE 8 Schematic of the design and preparation of piezoelectric catalytic antibacterial insole for wound healing.

material and biological studies have shown that the insole is biocompatible, exhibits stable performance, is cost-effective, and can improve the antibacterial and healing of infected wounds. The application of ultrasound and reciprocating machine impacts (to simulate walking) both serve as effective stress sources to stimulate the ferroelectric material within the insole to generate charge and an electric field. First, the use of the PDMS-BT ferroelectric composites effectively generates ROS (•OH, $•O_2^-$) through a ferroelectric-catalytic effect to increase the bacterial oxidative stress, reduce bacterial activity by nearly 80% and limit bacterial biofilm formation by nearly 75%. In addition, the ferroelectric field generated by the PDMS-BT, by affecting the endogenous electrical field within a wound, enhances the expression and secretion of TGF-β and CD31, thereby accelerating the migration of fibroblasts and angiogenesis, leading to an average wound healing area of 94% after 9 days. Unlike existing technologies, the performance of the ferroelectric antibacterial insole can be responsive to mechanical loads associated with foot pressure during walking, thereby eliminating the need for consumers to invest heavily in both time and resources. As a result, this work can inspire the design of other ferroelectric-based biomaterials used for antibacterial and tissue reconstruction.

4 | EXPERIMENTAL SECTION

4.1 | Reagents

Barium titanate ($BaTiO_3$, 99.9%; Macklin) was used as the raw ferroelectric material. PDMS and a curing agent were purchased from Dow Corning DC184 and used as the matrix material of the insole. The reagents involved in in vitro cell experiments include: HaCats and L929 cells were obtained from Xiangya Stomatological Hospital, human umbilical vein endothelial cells (HUVECs) were purchased from Chuanqiu Biotechnology Co., Ltd. Fetal bovine serum, Dulbecco's Modified Eagle Medium (DMEM) medium, RPMI1640, phosphate-buffered saline (PBS) and penicillin-streptomycin were purchased from VivaCell. A cell counting kit-8 (CCK-8) assay was used with the Elephant Innovation Center (EIC001A2351),

Calcein-acetoxymethyl ester/Propidium iodide (Calcein-AM/PI, E-CK-A354; Elabscience), Transwell cell culture plate (725001; NEST Biotechnology), Matrigel matrix (356234, Corning). *E. coli* strain (ATCC 25922; Beijing Biological Preservation Center), *S. aureus* (ATCC 25923; Beijing Biological Preservation Center) and Nutritional AGAR plate (HBPM003-6; HopeBio) were applied to the antibacterial experiments, Alamar Blue staining (A7631; Solarbio), ROS Assay Kit via DCFH-DA (Beyotime), crystal violet solution (G1062; Solarbio). In relation to animal experiments and histopathological studies, the following are relevant: Sprague Dawley (SD) rats purchased from TianQin Biotechnology, isoflurane (R510-22; RWD), TNF-β antibodies (WL02193; Wanleibio), and CD-31 antibodies (Abcam). All reagents unless otherwise stated were of the highest commercial grade available and were used directly without further purification.

4.2 | Fabrication of PDMS insole and PDMS/$BaTiO_3$ composite insole (PDMS-BT)

A mass of 0.4 g of curing agent was added to 10 g of PDMS, a mass fraction of 20% of barium titanate was used as the ferroelectric ceramic filler and mixed with PDMS evenly, where a homogeneous mixture was poured into the insole mould. The mould was placed into a vacuum drying oven and evacuated three to five times at room temperature to remove any air bubbles in the mixture. Finally, the mould was placed into a 60°C oven and cured for 2 h to obtain a ferroelectric ceramic-based antibacterial PDMS-BT insole with suitable hardness. The pure ferroelectric-free PDMS insoles were synthesized with the same method, but without $BaTiO_3$ added, as a control sample.

4.3 | Characterization

The specific details of characterization via SEM, XRD, infrared spectroscopy, XPS, FTIR and PFM of the samples are provided in the supporting materials.

4.4 | Cell experiment in vitro

4.4.1 | Cell culture and viability

HaCats and L929 cells were obtained from Xiangya Stomatological Hospital and cultured in high glucose DMEM medium with 10% fetal bovine serum (VivaCell) and 1% penicillin-streptomycin (VivaCell) in a humidified atmosphere containing 5% CO_2. The cells were seeded onto a transwell cell culture plate (725001; NEST Biotechnology), samples were cocultured in the lower chamber to evaluate the cytotoxicity in vitro. Ultrasound was applied to apply a high frequency mechanical load and produce a ferroelectric charge. The time for the groups to be exposed to US radiation was 10 min (1 MHz, 1.5 W cm^{-2}, WED-100; Shenzhen Well. d Medical Electronics Co., Ltd.). A cell counting kit-8 (CCK-8) assay was used with the Elephant Innovation Center (EIC001A2351) in accordance with the product specification to measure cell proliferation after 1, 3, and 5 days of coculture. The absorbance values were measured at 450 nm (OD450) using a microplate reader (BioTek).

In addition, the biocompatibility was further evaluated by live and dead cell staining. Briefly, HaCats and L929 cells were seeded in 24-well culture plates at the density of 2×10^4 cells per well, incubated for 24 h, and then cocultured with the samples for another 24 h. Afterward, the cells were stained with calcein-acetoxymethyl ester/propidium iodide for 30 min in the dark at 37°C and visualized by the inverted fluorescence microscope (Leica).

4.4.2 | Scratch assay

The effect of ultrasound exposure on cell migration was investigated by scratch assay according to standard protocols. Briefly, L929 cells were implanted into a six-well plate with a concentration of approximately 10^6/well and placed in an incubator for 24 h to reach 80%~90% confluence. After cell planking, a scratch was made with a sterilized 200 μL pipette tip. To make the remaining gap clearly visible, PBS was used to rinse the plates for three times to remove the falling cells. Then, the previous culture medium was replaced by serum-free RPMI-1640 after corresponding intervention (10 min US irradiation for the groups with ultrasound applied at 1 MHz, 1.5 W cm^{-2}). Experimental images were observed and captured with a microscope (Leica) after 0, 12, and 24 h of incubation, respectively. With the use of ImageJ Software, the scratch healing rate was determined by comparing the cell coverage at matching time periods in scratch.

4.4.3 | Angiogenesis

The angiogenic ability of HUVECs (Shanghai Chuanqiu Biotechnology Co.) in the different groups was evaluated by seeding cells on the Matrigel matrix (356234;

Corning). Briefly, the matrix was spread in a pre-cooled 96-well plate using precooled tips and solidified at 37°C for 30 min. Then 100 μL HUVECs suspension (2×10^5 cells mL^{-1}) was seeded on the matrix and incubated for 4 h. The number of tubules and number of junctions were measured by ImageJ with the Angiogenesis Analyzer plugin to assess the tubule formation ability.

4.5 | Antibacterial studies in vitro

4.5.1 | Plate-counting method

Gram-negative *E. coli* (ATCC 25922) and Gram-positive *S. aureus* (ATCC 25923) were used to test the antibacterial ability of the PDMS-BT. A plate-counting method was used to evaluate the antibacterial properties of different catalysts. Briefly, the PDMS-BT membrane was dispersed in 1 mL bacterial suspension (1×10^7 CFU mL^{-1}). After that, two methods were used to evaluate the antibacterial ability of materials by the application of a mechanical load. First, the bacterial suspension was subject to high frequency ultrasound (1 MHz, 2 W cm^{-2}, WED-100; Shenzhen Well. d Medical Electronics Co., Ltd.) for 20 min. Second, to more closely simulate the loading of the insole material during walking, the material and bacterial suspension were transferred to a sterile sealed bag, and then the hammer of the reciprocating machine (SYGFFK) was used to apply a mechanical load (1 Hz, 300 N). After gradient dilution, the bacterial suspensions were evenly coated on the agar plate (HBPM003-6; HopeBio) and cultured at 37°C for 24 h. And survival rate of bacteria were calculated by the following equation:

$$\text{Bacteria survival rate } (\%) = (C/C_0) \times 100,$$

where C was the bacteria colonies of the experiment groups, and C_0 was the number of the control group.

4.5.2 | Bacterial activity on material surface

The activity of *S. aureus* and *E. coli* on the surface of samples in each group was detected by Alamar Blue staining. After mixing the material with bacterial suspension for 24 h, US stimulation was used for 20 min, and then PBS was used to moisten and wash for three times. The test reagent was diluted 10 times and placed on a 24 well plate with the sample, incubated in an incubator at 37°C for 4 h, and tested at 590 nm with a microplate reader.

4.5.3 | Crystal violet biofilm staining

The sample was placed into each well of a 24-well plate that had 300 μL of 10^6 CFU mL^{-1} bacterial solution in it. Following a 10-min US stimulation session, the mixture was incubated for 24 h at 37°C. After removing the planktonic bacteria from the supernatant, the biofilm was washed three times with PBS. Subsequently, each well received 300 μL of methanol to fix the biofilm for 15 min. After the methanol was eliminated, the sample was dried in an oven set at 60°C. Subsequently, the biofilm was cultivated for 15 min using 200 μL of 1% crystal violet solution. Three PBS washes were used to remove excess crystal violet. Using a stereomicroscope, images were captured of the outcomes once they had dried at 60°C. Then, 200 μL of ethanol was added to each hole and shaken for 30 min using a shaker. The absorbance of each well bath solution at 570 nm (OD570) was measured by a microplate reader.

4.5.4 | Detection of ROS in bacteria

A 2′,7′-dichlorodihydrofluorescein diacetate (DCFH-DA) probe was used to investigate the level of ROS in bacteria. The bacteria after different treatments were stained with DCFH-DA (10 μM) for 0.5 h, followed by washing three times using PBS. After that, green fluorescence was observed using a fluorescence microscope (Leica) to examine the generation of ROS.

4.6 | In vivo antibacterial and wound healing

All surgical procedures were performed in strict accordance with Central South University guidelines for the care and use of laboratory animals and approved by the Animal Ethics Committee of Central South University (approval number: CSU-2023-0384). To assess the impact of PDMS-BT with US on infected wound healing, a full-thickness *S. aureus*-infected wound rat model (Sprague Dawley rats, 250–280 g, male) was used. Briefly, after continuous gas inhalation anaesthetization with 4% isoflurane using a noninvasive anesthesia apparatus (Beijing Zhongshi Dichuang Technology Development Co., Ltd.), each SD rat had a round skin ring drill-induced 8 mm diameter full-thickness cutaneous wound made on its back. In the next step, 10 μL of *S. aureus* suspensions (10^6 CFU mL^{-1}) were injected into the defected area to cause infection. After 24 h (recorded as Day 0), a routine swab culture and spread solid agar plate operation were performed to confirm wound infection.

Three groups were prepared, which were abbreviated as (i) control (US only), (ii) PDMS + US, and (iii) (PDMS-BT) + US respectively; where US is ultrasound. The wounds treated with only medical applications (i.e., medical dressing) and ultrasound represented the negative control group. For the other groups, the material was attached to the inner side of the medical dressing, which has an adhesive quality, allowing them to be applied to the wound as a single unit. Throughout this process, the material was in close contact with the surface of the wound while avoiding the application of excessive pressure. A low-sensitivity bandage (3M) was wound around the rat body for reinforcement. Different interventions were carried out on each wound (10 min US irradiation for the all groups with ultrasound, 1 MHz, 1.5 W cm^{-2}). We photographed the wound area on Days 0, 1, 3, 6, and 9 to monitor the healing process of an infected wound. The wound size was calculated by the following equation with ImageJ: The wound size (%) = (wound area on a specific day)/(wound area on Day 0) × 100%. Importantly, to ensure the objectivity of our analysis, all images were evaluated in a blinded manner by investigators who were not informed of the treatment groups, thereby minimizing any subjective bias in the wound size assessment.

4.7 | Histological analysis

To assess the healing of wounds and the regeneration of epidermis, sliced skin tissues were collected 9 days after treatment and processed for histological analysis. Specifically, the tissue samples were taken out, fixed with 4% paraformaldehyde for 1 h and then embedded in paraffin after dehydration. Serial sections with a thickness of 5 μm were obtained by microtome for H&E staining and Masson trichrome staining. The immunohistochemistry of TNF-β antibodies and CD-31 antibodies were performed following the manufacturer's instructions. In addition, to estimate the biocompatibility of the PDMS-BT in vivo, the major organs, including lung, liver, spleen, kidney and heart of SD rats were also obtained and sectioned for H&E staining. All images obtained from the above sections were recorded by a fluorescence microscope (Leica).

Quantitative data are expressed as means ± SDs. Statistical analyses were conducted using GraphPad Prism 9, with a minimum of three replicates per experiment to bolster the results' reliability. We employed the Student's t-test and one-way ANOVA for analyzing two and multiple group comparisons, respectively, after ensuring data normality and homogeneity of variances via the Shapiro-Wilk and Levene's tests. Tukey's post hoc test was utilized to discern intergroup differences. We determined statistical significance at levels of $*p < .05$, $**p < .01$, and $***p < .001$, and also reported effect sizes to provide insight into the magnitude of observed differences.

4.8 | 3D FEM simulation

A 3D finite-element model was set up in COMSOL Multiphysics®. In this model, the piezoelectric interface was constructed via a "Structural Mechanics Module" and contained both the BT domain and PDMS domain. The shape of the model was matched to the dimensions of the insole, and the BT particles were assumed to be fully embedded in the PDMS matrix.

ACKNOWLEDGMENTS

This work was financially supported by Hunan Excellent Youth Science Foundation (2022JJ20067), Scientific research project of Hunan Provincial Department of Education (21B0009), the National Natural Science Foundation of China (52172265, 5230130435), the State Key Laboratory of Powder Metallurgy, Central South University, Changsha, China, and the Hong Kong Polytechnic University (1-W34B). The authors also extend their gratitude to Shiyanjia Lab (www.shiyanjia.com) for providing invaluable assistance with the histopathological sections.

CONFLICT OF INTEREST STATEMENT

The authors declare no conflict of interest.

ORCID

Xudan Liu http://orcid.org/0000-0001-7619-2502
Dou Zhang http://orcid.org/0000-0001-8555-2784

REFERENCES

[1] Falanga V, Isseroff RR, Soulika AM, et al. Chronic wounds. *Nat Rev Dis Primers*. 2022;8(1):50.
[2] Falanga V. Wound healing and its impairment in the diabetic foot. *Lancet*. 2005;366(9498):1736–1743.
[3] Luo X, Zhang L, Luo Y, et al. Charge-driven self-assembled microspheres hydrogel scaffolds for combined drug delivery and photothermal therapy of diabetic wounds. *Adv Funct Mater*. 2023;33(26):2214036.
[4] Li Y, Fu R, Guan Y, et al. Piezoelectric hydrogel for prophylaxis and early treatment of pressure injuries/pressure ulcers. *ACS Biomater Sci Eng*. 2022;8(7):3078–3086.
[5] Roldan L, Montoya C, Solanki V, et al. A novel injectable piezoelectric hydrogel for periodontal disease treatment. *ACS Appl Mater Interfaces*. 2023;15(37):43441–43454.
[6] Tai G, Tai M, Zhao M. Electrically stimulated cell migration and its contribution to wound healing. *Burns Trauma*. 2018;6:20.
[7] Yu C, Xu ZX, Hao YH, et al. A novel microcurrent dressing for wound healing in a rat skin defect model. *Mil Med Res*. 2019;6(1):22.

[8] Kim SW, Cho S, Lee D, et al. Inhibiting scar formation via wearable multilayer stacked electret patch: self-creation of persistent and customizable DC electric field for fibrogenic activity restriction. *InfoMat*. 2023;6:e12489.
[9] Lin J, Fu R, Zhong X, et al. Wearable sensors and devices for real-time cardiovascular disease monitoring. *Cell Rep Phys Sci*. 2021;2(8):100541.
[10] Liu D, Li L, Shi BL, et al. Ultrasound-triggered piezocatalytic composite hydrogels for promoting bacterial-infected wound healing. *Bioact Mater*. 2023;24:96–111.
[11] Wu M, Zhang Z, Liu Z, et al. Piezoelectric nanocomposites for sonodynamic bacterial elimination and wound healing. *Nano Today*. 2021;37:101104.
[12] Zhao X, Wang LY, Tang CY, et al. Electro-microenvironment modulated inhibition of endogenous biofilms by piezo implants for ultrasound-localized intestinal perforation disinfection. *Biomaterials*. 2023;295:122055.
[13] Zhang M, Wang Y, Liu J, et al. Facile one-step synthesis and enhanced photocatalytic activity of a WC/ferroelectric nanocomposite. *J Mater Chem A*. 2021;9(40):22861–22870.
[14] Chen J, Song L, Qi F, et al. Enhanced bone regeneration via ZIF-8 decorated hierarchical polyvinylidene fluoride piezoelectric foam nanogenerator: coupling of bioelectricity, angiogenesis, and osteogenesis. *Nano Energy*. 2023;106:108076.
[15] Luo R, Liang Y, Yang J, et al. Reshaping the endogenous electric field to boost wound repair via electrogenerative dressing. *Adv Mater*. 2023;35(16):e2208395.
[16] Wang Y, Wen X, Jia Y, et al. Piezo-catalysis for non-destructive tooth whitening. *Nat Commun*. 2020;11(1):1328.
[17] Masekela D, Hintsho-Mbita NC, Sam S, Yusuf TL, Mabuba N. Application of $BaTiO_3$-based catalysts for piezocatalytic, photocatalytic and piezo-photocatalytic degradation of organic pollutants and bacterial disinfection in wastewater: a comprehensive review. *Arab J Chem*. 2023;16(2):104473.
[18] Wang Y, Zhang M, Liu J, et al. Domain wall free polar structure enhanced photodegradation activity in nanoscale ferroelectric $Ba_xSr_{1-x}TiO_3$. *Adv Energy Mater*. 2020;10(38):2001802.
[19] Dai B, Zhang L, Huang H, Lu C, Kou J, Xu Z. Photocatalysis of composite film PDMS-PMN-PT@TiO_2 greatly improved via spatial electric field. *Appl Surf Sci*. 2017;403:9–14.
[20] Masimukku S, Hu YC, Lin ZH, Chan SW, Chou TM, Wu JM. High efficient degradation of dye molecules by PDMS embedded abundant single-layer tungsten disulfide and their antibacterial performance. *Nano Energy*. 2018;46:338–346.
[21] Singh G, Sharma M, Kiran R, Karmakar S, Vaish R. Footwear for piezoelectric energy harvesting: a comprehensive review on prototypes development, applications and future prospects. *Curr Opin Solid State Mater Sci*. 2024;28:101134.
[22] Liu Q, Zhan F, Luo H, et al. Mechanism of interface engineering for ultrahigh piezo-photoelectric catalytic coupling effect of $BaTiO_3$@TiO_2 microflowers. *Appl Catal B*. 2022;318:121817.
[23] Ravizza E, Spadoni S, Piagge R, Comite P, Wiemer C. XPS composition study of stacked Si oxide/Si nitride/Si oxide nano-layers. *Surf Interface Anal*. 2012;44(8):1209–1213.
[24] Meškinis Š, Andrulevičius M, Tamulevičius S, et al. XPS study of the a-C:H/Ti and a-C:H/a-Si interfaces. *Vacuum*. 2006;80(9):1007–1011.
[25] Armyanov S, Stankova NE, Atanasov PA, et al. XPS and μ-Raman study of nanosecond-laser processing of poly(dimethylsiloxane) (PDMS). *Nucl Instrum Methods Phys Res Sect B Beam Interact Mater Atoms*. 2015;360:30–35.
[26] Yu Y, Xu G, Zhao P, Zhang J. Biocompatible, robust, waterproof and breathable PDMS-based PU fibrous membranes for potential application in wound dressing. *Mater Today Commun*. 2024;38:107870.
[27] Genchi GG, Marino A, Rocca A, Mattoli V, Ciofani G. Barium titanate nanoparticles: promising multitasking vectors in nanomedicine. *Nanotechnology*. 2016;27(23):232001.
[28] Mao G, Tian S, Shi Y, et al. Preparation and evaluation of a novel alginate-arginine-zinc ion hydrogel film for skin wound healing. *Carbohydr Polymers*. 2023;311:120757.
[29] Wang Y, Liu KK, Zhao WB, et al. Antibacterial fabrics based on synergy of piezoelectric effect and physical interaction. *Nano Today*. 2023;48:101737.
[30] Bai Q, Zhang J, Yu Y, et al. Piezoelectric activatable nanozyme-based skin patch for rapid wound disinfection. *ACS Appl Mater Interfaces*. 2022;14(23):26455–26468.
[31] Zhou L, Li H, Zhang X, et al. Rapamycin treated tol-dendritic cells derived from BM-MSCs reversed graft rejection in a rat liver transplantation model by inducing $CD8^+$CD45RC-Treg. *Mol Immunol*. 2021;137:11–19.
[32] Liu H, Qu X, Kim E, et al. Bio-inspired redox-cycling antimicrobial film for sustained generation of reactive oxygen species. *Biomaterials*. 2018;162:109–122.
[33] Chen X, Li X, He W, et al. Rational multivalency construction enables bactericidal effect amplification and dynamic biomaterial design. *Innovation*. 2023;4(5):100483.
[34] Fu R, Zhong X, Xiao C, et al. A stretchable, biocompatible, and self-powered hydrogel multichannel wireless sensor system based on piezoelectric barium titanate nanoparticles for health monitoring. *Nano Energy*. 2023;114:108617.
[35] Zhang Y, An Q, Zhang S, et al. A healing promoting wound dressing with tailor-made antibacterial potency employing piezocatalytic processes in multi-functional nanocomposites. *Nanoscale*. 2022;14(7):2649–2659.
[36] Wu L, Luo Y, Wang C, et al. Self-driven electron transfer biomimetic enzymatic catalysis of bismuth-doped PCN-222 MOF for rapid therapy of bacteria-infected wounds. *ACS Nano*. 2023;17(2):1448–1463.
[37] Kai H, Yamauchi T, Ogawa Y, et al. Accelerated wound healing on skin by electrical stimulation with a bioelectric plaster. *Adv Healthc Mater*. 2017;6(22):1700465.
[38] Huang R, Zhang X, Li W, Shang L, Wang H, Zhao Y. Suction cups-inspired adhesive patch with tailorable patterns for versatile wound healing. *Adv Sci*. 2021;8(17):e2100201.
[39] Fu R, Tu L, Zhou Y, et al. A tough and self-powered hydrogel for artificial skin. *Chem Mater*. 2019;31(23):9850–9860.
[40] Su C, Li R, Li C, Wang W. Piezo-promoted regeneration of Fe^{2+} boosts peroxydisulfate activation by $Bi_2Fe_4O_9$ nanosheets. *Appl Catal B*. 2022;310:121330.
[41] Lin E, Kang Z, Wu J, Huang R, Qin N, Bao D. $BaTiO_3$ nanocubes/cuboids with selectively deposited Ag nanoparticles: efficient piezocatalytic degradation and mechanism. *Appl Catal B*. 2021;285:119823.

[42] Li L, Gu W, Du J, et al. Electric fields guide migration of epidermal stem cells and promote skin wound healing. *Wound Repair Regen*. 2012;20(6):840–851.

SUPPORTING INFORMATION

Additional supporting information can be found online in the Supporting Information section at the end of this article.

How to cite this article: Liu Q, Liu X, Fan L, et al. Ferroelectric catalytic $BaTiO_3$-based composite insoles to promote healing of infected wounds: analysis of antibacterial efficacy and angiogenesis. *Interdiscip Mater*. 2024;3:757–774. doi:10.1002/idm2.12194